Experimental Mechanics (2022) 62:849–862
https://doi.org/10.1007/s11340-022-00819-9

RESEARCH PAPER

Effect of Confinement on the Impact Response of a Granular Array

R. D. J. I. Fonseka[1] · **P. H. Geubelle**[1] · **J. Lambros**[1]

Received: 10 June 2021 / Accepted: 3 January 2022 / Published online: 31 March 2022

Abstract

Background Plastic dissipation at inter-granular contacts during elasto-plastic wave propagation plays a significant role in wave attenuation. However, it is unknown if plastic dissipation during impact is enhanced if the granular medium is initially in an unconfined 'fluid-like' state or that of a more rigid 'solid-like' state caused by applying a confining pressure.

Objective The goal of this work is to investigate both experimentally and numerically the impact response of a two-dimensional hexagonal granular array consisting of metallic spheres enclosed in a polymeric membrane subjected to different levels of confining pressure. We seek to quantify the granular trajectories, the effect of the membrane, and the ratio of the dissipated plastic energy to the net input energy between the unconfined and confined states.

Methods We perform experiments using a modified split Hopkinson pressure bar on a specimen of monodisperse brass spheres confined by a polymeric membrane and record the impact event using high-speed photography so that particle tracking can be used to track granular motion. After impact, the sphere surfaces are examined to measure plastic contact areas, allowing the dissipated plastic energy to be estimated. To support the experiments, capture the lateral confining effect of the membrane and applied pressure, and investigate larger arrays, discrete element simulations are conducted.

Results When the granular array is confined, we observed shorter and consistent granular trajectories between trials, a greater dissipated energy to net input energy ratio, and a stiffer membrane response.

Conclusion Experimental and numerical results indicate that the external confining pressure increases plastic dissipation.

Keywords Granular media · Impact · Plastic dissipation · Particle Tracking

Introduction

The unique wave propagation properties of granular media and their versatility based on size distribution and granular characteristics have sparked interest in the use of granular media for impact mitigation. Research done in the past two decades has shown that by simply tapering a granular chain or by adding heterogenities to the chain in the form of granules with different sizes and/or material properties, one can severely attenuate nonlinear solitary waves which traverse granular systems [1–3]. Further attenuation can be achieved by splitting the input energy along multiple granular pathways or transferring energy to supporting structures such as elastic membranes and guides [4–6]. It is important to note that most of these methods do not require dissipation at the contact-level such as viscoelasticity, friction and plastic deformation to mitigate impact. However, the inclusion of contact level dissipation has been shown to be very effective in dissipating energy without the need for complex structuring or arrangement of granules. Viscoelastic interactions for example can have coefficients of restitution which continue to decrease with impact velocity thereby enabling less energy to be transferred from one granule to another [7, 8]. Energy can also be dissipated by friction due to the relative motion and rotation of the granules during an impact event [9, 10]. For higher levels of loading, plastic deformation at contacts can also take place in ductile granules. In general, the contact-induced stress concentrations cause the granules to yield at low globally applied loads, thereby attenuating waves more efficiently than in the bulk material, which would have remained elastic for the same load [11].

✉ J. Lambros
lambros@illinois.edu

R. D. J. I. Fonseka
fonseka2@illinois.edu

P. H. Geubelle
geubelle@illinois.edu

[1] 306 Talbot Laboratory, MC-236, 104 S. Wright St, Urbana, IL 61801, USA

By understanding the parameters that control these relative energy dissipation mechanisms, we can design devices with superior mitigation capabilities.

One relatively unexplored feature in the design of an impact protection granular system is achieving mitigation by controlling the amount of plastic dissipation at contacts. The tunable parameter we investigate is the level of confinement which can be varied by altering the external pressure confining the granular array. When the array is unconfined and in a hexagonal close pack (90.6% packing fraction in 2D), the granules are free to move laterally and are only resisted by their enclosure. However, an external confining pressure adds a precompression which resists granular motion therefore adds rigidity to the array without changing the packing fraction. This solid-like response contrasts with that of the unconfined state in which the lack of force chains makes the granules flow like a liquid when subjected to shear loading. One would therefore expect that this difference in material response translates to a transition in energy dissipation mechanisms from a friction-dominated mechanism in the unconfined case to a plasticity-driven dissipation process in the confined state. The focus of this paper is to investigate the effect the confining pressure has on plastic dissipation.

To fully understand the mechanisms involved in an impact event, it is imperative to understand wave propagation in granular media. Seminal work began with the identification of nonlinear amplitude dependent elastic solitary waves in 1D uncompressed chains using a Hertzian contact law between granules [12]. Subsequently, it was found that precompressing granular systems can give a mix of linear and nonlinear wave propagation behavior depending on the ratio of precompression to dynamic loading, with wave propagation becoming increasingly linear with precompression [13–17]. Studies were then extended to chains with dimers [18, 19], 2D packings [20], and different loading conditions for 2D and 3D packings [21, 22]. However, these results are limited to loads within the elastic regime, which are much less than the loads generated during high-energy impact. In the plastic regime, the contact law deviates from the Hertzian contact law to an elasto-plastic contact law. Pioneering experiments performed by Shukla and coworkers on disks highlight this effect by showing that wave propagation can be accurately described by using a deformation-dependent damping contact law [23, 24]. Experimental studies on spheres have shown that the transmitted energy at the inter-granular contacts under impulsive elasto-plastic conditions is dependent on the material properties, impact velocity, and diameter ratios of the granules [25, 26]. Experiments on 1D chains and 2D granular packings have found that the shape of the output pulse significantly attenuates with distance when compared with the loading pulse and depends on the packing configuration [27–30]. These experimental results are validated by simulations which used analytical or numerically obtained elasto-plastic contact laws between granules.

In this study, we evaluate the impact response of a granular array that consists of brass spheres enclosed in a polymeric membrane subjected to vacuum by quantifying the effect the vacuum pressure has on the ratio of dissipated plastic energy to input energy and on the trajectories of the impacted grains. When vacuum is applied, the pressure difference causes the granules to transition to a more rigid state. This transition is used, for example, in soft robotics application to grip and move objects [31, 32]. The overall rigidity of the assembly can be tuned by changing the vacuum pressure with lower absolute pressures (i.e., higher vacuum) resulting in increased solidity. Previous studies have shown the role of the membrane in increasing the overall stiffness of the structure [32] and storing energy during impact in the form of strain energy [5].

To investigate the energy dissipation mechanisms in the unconfined and confined states, we conduct split Hopkinson pressure bar-like (SHPB) experiments on brass specimens and study the effect of the applied vacuum on the motion of the granules and the associated plastic energy dissipation. High-speed photography and particle tracking are used to extract the trajectories and kinematics of the spheres during impact. After impact, the bead surfaces are examined to quantify the energy dissipated due to plasticity. These experimental methods are described in Experimental Setup. To support the experiments, we detail in Numerical Method Discrete Element Method (DEM) simulations used to model the influence of the membrane, make comparisons with experimental measurements, and investigate the scaling of results with arrays of larger sizes. The results and discussion of the experimental and simulation results are presented in Results and Discussion.

Experimental Setup

The specimens used for this experiment consist of 9.52 *mm*-diameter brass 260 spheres obtained from McMaster-Carr, which are arranged in a 5x5 hexagonal packing inside of a membrane made of Stretchlon 200 bagging film. A 5x5 packing was chosen as it shows the lateral expansion of the array within the confines of the experimental setup unlike larger arrays which inhibit this motion or touch the sides of the testing rig. Additionally, the meticulous process of tabulating the plastic dissipation for all the contacts also limits the use of a lot of granules. Stretchlon 200, commonly used in the vacuum-assisted resin-transfer molding of composites, was selected as the membrane in these experiments because it can stretch as much as 500%, thereby allowing it to conform to the granules and resist failure during impact. Confinement is induced by the suction of air from the bag

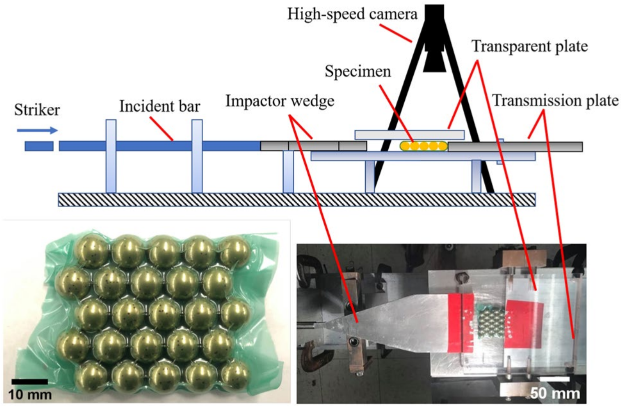

Fig. 1 Split Hopkinson pressure bar setup and an enlarged image of the granular specimen subjected to 100 *kPa* vacuum pressure

using a vacuum pump. Since the spheres are monodisperse and are prearranged in a hexagonal packing prior to applying vacuum, the spheres attain the densest packing of a hexagonal close pack once confined. To maintain consistency, bag dimensions are chosen to enclose a hexagonal array without excess material.

The experimental setup consists of a modification of a SHPB to load the granular array, which rests on a steel testing rig as shown in Fig. 1. The setup consists of an incident bar, which impacts an aluminum wedge-shaped plate that in turn impacts the specimen across its entire width. On the opposite side of the loading, the specimen contacts a fixed steel plate which acts as a rigid support. A transparent plexiglass plate is placed on top of the array to prevent out of plane motion of the granules and to allow for the experiment to be viewed from above using a high-speed camera. The array lies on top of a steel plate and is aligned such that the centerline of the array coincides with the center of the wedge.

A Redlake HS-4 high-speed camera is used to capture loading and unloading at a frame rate of 11600 *fps* (time between frames of 0.086*ms*) with a resolution of 480 by 224 pixels. This frame rate is too low to capture initial elasto-plastic wave propagation through the array occurring over 0.08*ms* [27] but provides a sufficient temporal resolution to view the motion of all the granules during longer times, and their interaction with the membrane. Selected frames of the different phases of the experiment are shown in Fig. 2 for experiments without a membrane (Fig. 2(a)), unconfined with membrane (Fig. 2(b)), and confined at 100 *kPa* (Fig. 2(c)). A particle-tracking Python library, Trackpy [33], was used to track the motion of the granules by detecting the location of light reflection off individual granules. These reflections manifest as bright circles, which contrast against a dark background, thereby making it possible for the particle tracking algorithm to detect and track trajectories. Using this information, it is possible to determine the horizontal (x) and vertical (y) displacements of the granules. Consequently, their respective horizontal and vertical velocities can be found by fitting a cubic spline to the displacement histories and taking the time derivative.

In a conventional SHPB setup, the energy input into the system can be determined using the incident and reflected pulse signals in the incident bar. However, in our setup, the presence of a loading wedge between the incident bar and specimen implies that the incident bar pulse signal is not

Fig. 2 Selected sequence of high-speed images of the experiment for (**a**) no membrane, (**b**) unconfined with membrane, and (**c**) confined at 100 *kPa*. The scale bar is uniform throughout all images and 0*s* corresponds to the time at impact. The left, center, and right set of frames respectively capture the pre-impact, loading, and unloading part of the impact event

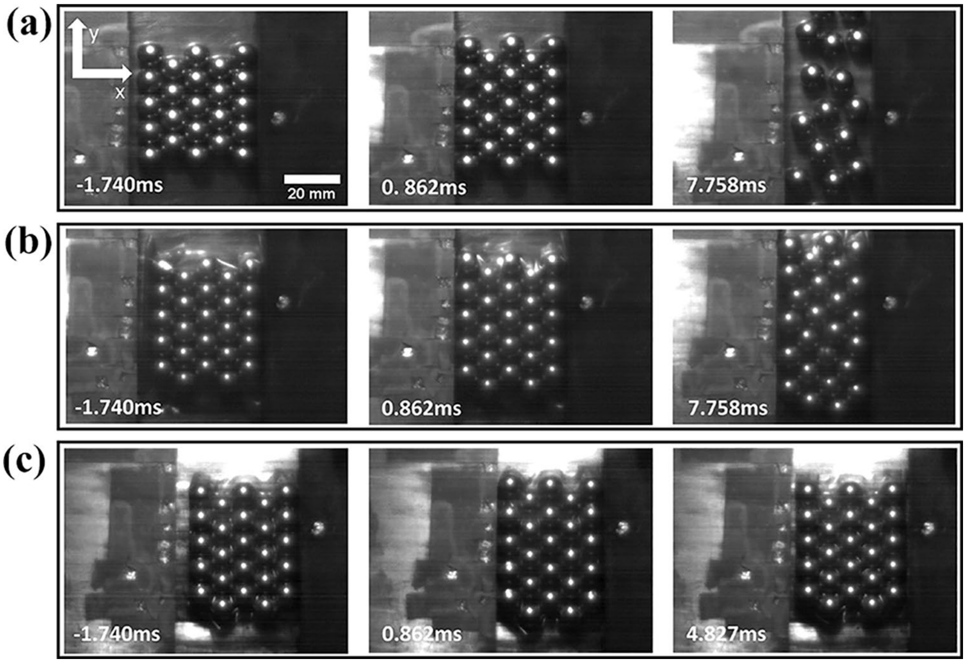

representative of the loading that enters the granular array. To address this issue, a small gap is left between the wedge and the array at the start of each experiment so there is enough time for the wedge to move as a rigid body. The position of the loading wedge is tracked by detecting the light reflected by aluminum foil placed on the wedge surface. The wedge is assumed to move rigidly at this longer time scale and the input energy is the kinetic energy of the wedge right before impact. Frictional losses between the wedge and the steel surface along which it moves are assumed to be negligible for the distance traveled by the wedge as verified by experiments in the absence of granular specimens. The fixed transmission plate to the rear of the specimen does not move during the impact event as verified by Trackpy.

Finally, after the experiment was completed, we quantified how much of the input energy was dissipated as plastic energy at the granule contact points by examining the granules visually using a stereo microscope and by photographing all visible dimples. Note that the granular surfaces were also examined prior to each experiment. If any pre-existing dimples were detected, the granules were either discarded or not included in the final tally. It should be noted that dimples are not generated during the confining process as confirmed by inspecting the granular surface after confining the array in the vacuum bag and then removing from the bag without loading. Typically, the dimples were circular or oblong in nature, and, less than 5% of all the dimples showed multiple overlapping dimples at the same location, which would indicate repeated impacts. Dimples in an image (Fig. 3(a)) were detected using the elliptical Hough transform algorithm [34]. The ellipse's major and minor dimensions were averaged to obtain the dimple diameter of an equivalent circle. For overlapping dimples in the 5% of cases, an ellipse was fitted to encompass both dimples as shown in Fig. 3(b). This approach was adopted because the region of overlap between dimples deformed elastically, and accounting for the dissipated energy of both dimples individually would greatly overestimate the dissipated energy. Similarly, it should also be noted that repeated collisions at the same dimple would not continue to dissipate additional plastic energy once the largest dimple diameter is attained.

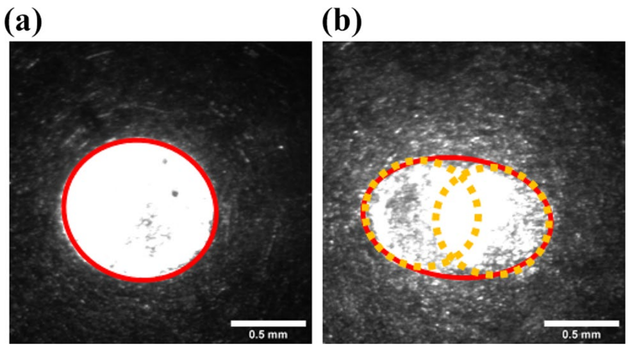

Fig. 3 (**a**) Single dimple and (**b**) multiple dimples at a contact. The gold outline in (**b**) demarcates the individual dimples, while the red outline denotes the fitted ellipse to compute the averaged dimple diameter

Numerical Method

Contact Law

The contact force between two granules is governed by the contact law derived from FEM simulations by Pal et al. [35] for sphere-sphere contact with rate-independent and elastic-perfectly-plastic material properties. The relation between the force (F) between contacting granules and the relative displacement (δ) between them is expressed in three stages: (i) elastic Hertzian contact, (ii) plastic loading to the maximum force (F_{max}), and (iii) elastic unloading to a permanently deformed state with a residual displacement (δ_r). Subsequent reloading follows the elastic unloading contact relationship until F_{max} with any further loading beyond this point following the plastic contact law. In the loading phase, the contact force, F_l, takes the following form:

$$F_l = \begin{cases} \frac{4}{3}E^* \sqrt{R^* \delta^3}, & \delta \le \delta_y, \\ \sigma_y A_y \left(2.48 - 1.41 \exp\left(-0.098\left(\frac{\delta}{\delta_y} - 1\right)\right)\right)\left(\frac{A}{A_y}\right) & \delta \ge \delta_y \end{cases} \tag{1}$$

with

$$\frac{A}{A_y} = \begin{cases} \left(\frac{\delta}{\delta_y}\right)^{1.14}, & \delta_y \le \delta \le 177.6\delta_y \\ \left(2.37\left(\frac{\delta}{\delta_y}\right) - 59.96\right), & \text{otherwise} \end{cases} \tag{2}$$

where the normal displacement at yield, δ_y, and the contact area at yield, A_y, are respectively given by $\delta_y = \frac{1}{4}\left(\frac{1.6\pi\sigma_y}{E^*}\right)^2 R^*$ and $A_y = \pi R^* \delta_y$. During unloading, the contact force, F_u, is expressed as

$$F_u = F_{\max}\left(\frac{\delta - \delta_r}{\delta_{\max} - \delta_r}\right)^{1.35}, \tag{3}$$

where

$$\delta_r = 0.95\delta_{\max} - 25.94\delta_y + 25 \exp\left(-0.015\left(\frac{\delta_{\max}}{\delta_y} - 1\right)\right)\delta_y.$$

E^* and R^* are the effective Young's modulus and effective radius, respectively, and are given by

$$E^* = \left(\frac{1 - \nu_1^2}{E_1} + \frac{1 - \nu_2^2}{E_2} \right)^{-1} \quad \text{and} \quad R^* = \left(\frac{1}{R_1} + \frac{1}{R_2} \right)^{-1}.$$

The pertinent material properties for brass are: Young's modulus $E = 115\ GPa$, Poisson's ratio $\nu = 0.3$, and yield stress $\sigma_y = 619\ MPa$ [25]. The subscripts 1 and 2 distinguish the properties of the two contacting granules.

The impactor wedge and transmission plate are modeled as rigid half-spaces, and their interaction with the brass granules in the loading phase is approximated by doubling the contact force corresponding to a given relative displacement as shown in equation (1). It should be noted that this approximation for the contact law may not be directly applicable as the wedge is made out of aluminum, which has a lower yield strength than brass. However, we found that changing the parameters of the wedge did not yield drastic differences in the grain trajectories or the wedge velocity, and showed a good agreement with the experiments as seen in Fig. 10. The unloading phase follows equation (3) with the residual displacement, $\delta_{r,wall}$, given as

$$\delta_{r,wall} = \delta_{max} - \left(\frac{3F_{max}}{4E^*_{wall} R^*_p} \right). \tag{4}$$

Here the residual effective radius, R^*_p, can be found using

$$R^*_p = \frac{4E^*_{wall}}{3F_{max}} \left(\frac{2F_{max} + 2F_{y,wall}}{2\pi(4.7)\sigma_y} \right)^{1.5}, \tag{5}$$

where E^*_{wall} and $F_{y,wall}$ are respectively the equivalent stiffness and yield force assuming the wall is rigid. Equations (4–5) is obtained from the analytical Thornton model for the elastic-perfectly-plastic contact of two spheres, which was shown to approximate interactions between a sphere and a wall reasonably well [36]. The contact laws between brass beads and between a brass bead and the rigid half space are presented in Fig. 4, together with the (elastic) Hertzian contact relation shown for reference. By relating the force, the relative displacement, and the residual displacement to the contact area, A, equations (1–3) allows for the evaluation of the dissipated plastic energy, E_p, as the area between the loading and unloading curves in Fig. 4(a) as

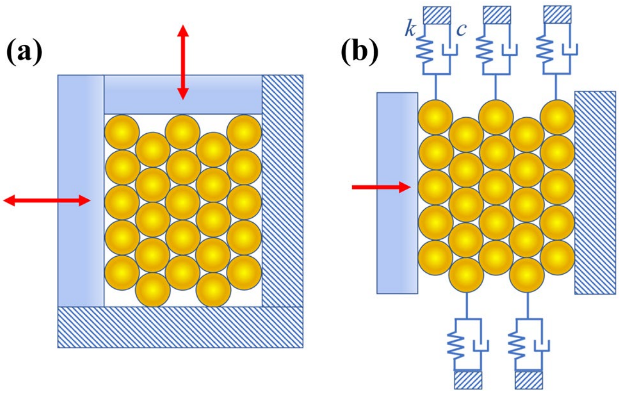

Fig. 5 Schematic for numerical simulations: (**a**) quasi-static confinement and (**b**) impact simulation. Striped walls are stationary while filled walls can move in the direction of the arrows

$$E_p = \int_0^{\delta_{max}} F_l \mathrm{d}\delta - \int_{\delta_r}^{\delta_{max}} F_u \mathrm{d}\delta. \tag{6}$$

The dissipated plastic energy E_p can thus be extracted given the dimple diameter using the curve in Fig. 4(b).

Quasi-static Confinement Simulations

Confinement is achieved in the simulations by compressing the granules in a quasi-static manner by using movable rigid walls surrounding the granules as illustrated in Fig. 5(a). In this process, the motion of the walls is progressively imposed so that the equivalent stress state of the discrete system given by equation (7), corresponds to a state of hydrostatic pressure with amplitude corresponding to the applied vacuum pressure. The volume-averaged stress tensor is given by

Fig. 4 (**a**) Elasto-plastic contact law for brass sphere-sphere interaction (red) and sphere-rigid-wall interactions (blue) compared with the classical Hertzian contact law (green). (**b**) Dissipated plastic energy, E_p, versus the dimple diameter

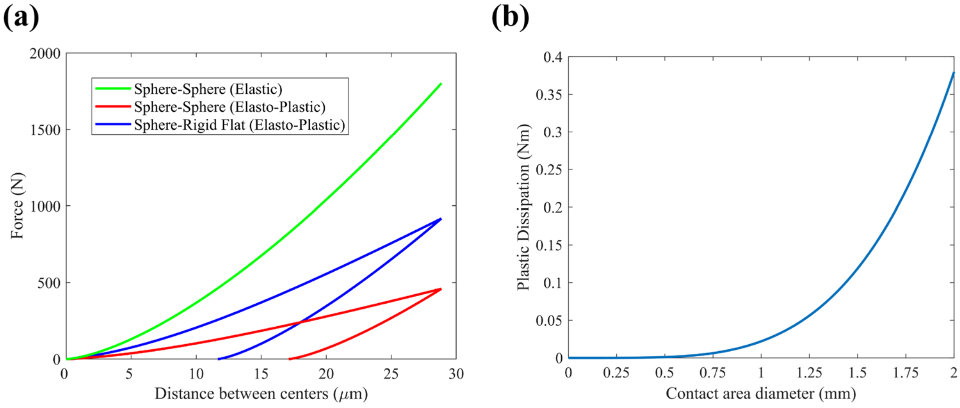

$$\sigma_{\alpha\beta} = \frac{1}{V}\sum_{c=1}^{N_c} f_\alpha^c l_\beta^c, \tag{7}$$

where f_α^c and l_β^c are the force and branch vectors, respectively, at contact c, and the product is summed over all contacts, N_c [37]. For a given granule i contacting n_i neighboring granules, equilibrium equations can be written as

$$\sum_{j=1}^{n_i} \mathbf{F}_{i,j} + \mathbf{R}_i = 0, \tag{8}$$

where $\mathbf{F}_{i,j}$ is the contact force vector between granule i and contacting granule j, and $\mathbf{R}_i$ is the wall reaction force vector acting on granules along the boundary. Expanding equation (8) for all the granules gives a system of coupled nonlinear equations, which are solved using the Newton-Raphson method at every increment of wall compression for the unknown granular centroid locations and boundary reaction forces.

Impact Simulations

Impact simulations are performed using the discrete element method with the equations of motion solved in the x and y directions for the system shown schematically in Fig. 5(b). The impactor wedge, denoted by the left wall in Fig. 5(b), and the transmission plate, corresponding to the right wall in Fig. 5(b), are modelled as rigid steel particles with infinite radii. To match the experiments, the impactor wedge is given the experimentally measured mass while the rigid wall is assumed to have an infinite mass. In addition, the wedge is constrained to move only in the x direction. The initial velocity of the wedge is set as the value measured experimentally using particle tracking. The granules are initially assumed to be at rest with centroidal positions and reaction forces obtained from the confining simulations described in Quasi-static Confinement Simulations. The reaction forces are exerted throughout the simulation and continue to act on the granules along the upper and lower boundaries. In this simplified numerical analysis, only normal, frictionless, elasto-plastic contact is modelled and rotational effects are neglected.

To further simplify the computational model, the membrane itself is not explicitly modelled but rather the primary effects of the membrane are simulated using a simplified spring-dashpot model with stiffness, k, and dissipation coefficient, c, linked to the lateral (free) surfaces of the granular array as shown in Fig. 5(b). The linear spring of stiffness k represents the stiffness of the membrane and the dashpot of coefficient c captures dissipation due to the motion of the granules against the conforming membrane. The values of k and c are calibrated through comparison with experiments using a parametric study described in Calibration of Membrane Properties.

The equations of motion for all the granules yield a system of ordinary differential equations in terms of the position of the centroid of granules, which are solved using the fourth-order Runge-Kutta scheme. A timestep of $5 \times 10^{-8} s$ was chosen after a convergence study on numerical values generated in the simulation.

Results and Discussion

Trajectory and Kinematics

As reflected in Fig. 6, the granular trajectories for the different experimental scenarios are the following: without membrane; unconfined (no vacuum pressure but enclosed in membrane); and confined with 50, 70, and 100 kPa vacuum pressure. In the absence of a membrane (Fig. 6(a)), the unrestrained granules rapidly lose contact with their neighbors and follow linear trajectories. As expected, experiments performed with the membrane (Fig. 6(b–e)) yield granule trajectories with much smaller displacements, especially with the application of vacuum. The repeatability of the experimental results increases with the level of confinement due to the combined effect of the stiffening of the membrane and the equilibration of the crystal into a hexagonal close pack configuration. The added variability in the unconfined specimen can also be attributed to the presence of small gaps at contacts as noted in previous experiments [30]. It is also worth observing that granules in the confined experiments return to their pre-impact arrangements after unloading, while the unconfined crystal undergoes a substantial rearrangement as seen in Fig. 2(a).

The vertical (y) and horizontal (x) velocities obtained by differentiating the trajectory data with time are presented in Fig. 7 and show a strong acceleration in both directions in the initial phase of the impact event, followed by a rapid deceleration to an instantaneous rest at maximum compression. The horizontal velocity then switches sign and the granules return to their original position at a slower velocity. Even though the results presented in Fig. 7 correspond to a 70 kPa experiment, profiles with similar features are found for other vacuum pressures.

The measured evolution of the wedge velocity, which is used as one of the key validation quantities in the numerical analysis presented in the next section, is shown in Fig. 8 for different values of the confining pressure. The wedge rapidly decelerates after impact until it momentarily loses contact with the specimen as apparent by the kink early in the profile. This temporary separation is attributed to the reflected primary wave from the transmission plate impacting the wedge. As also apparent in Fig. 8, the wedge velocity

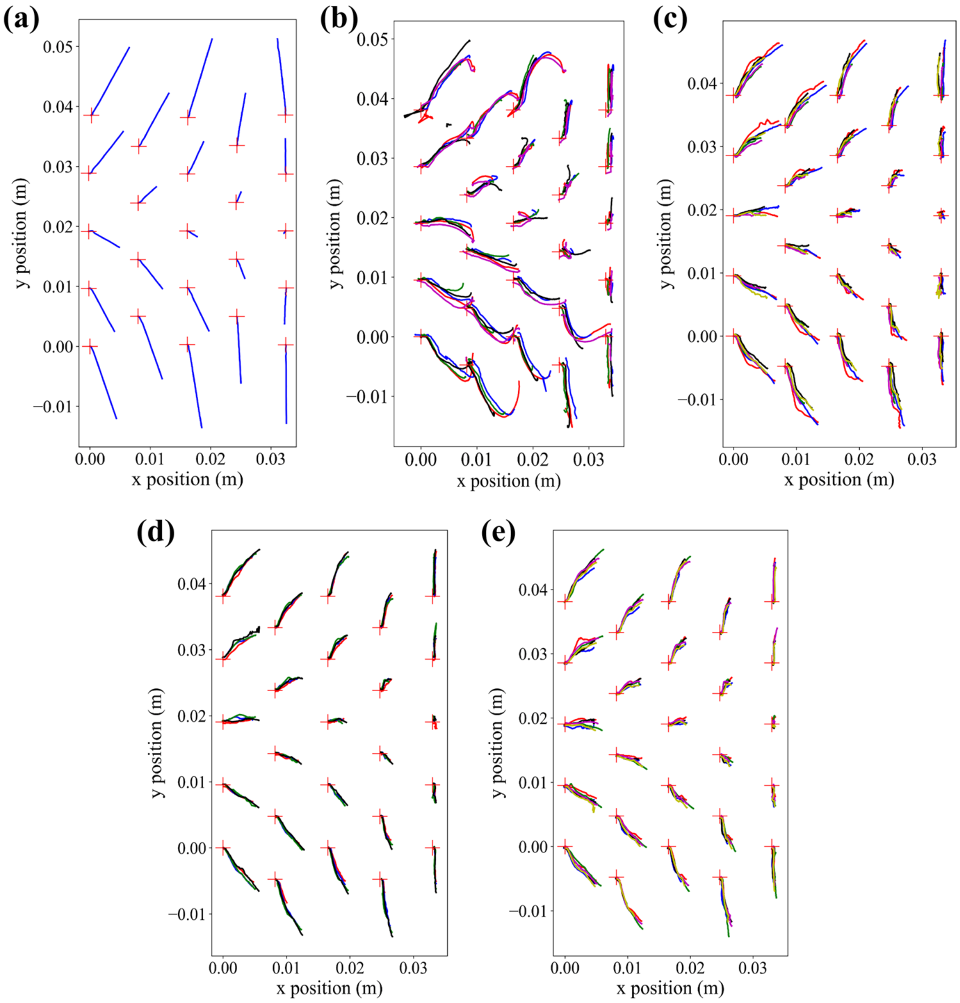

Fig. 6 Experimental granular trajectories for (**a**) no membrane, (**b**) unconfined, (**c**) 50 *kPa*, (**d**) 70 *kPa*, and (**e**) 100 *kPa* vacuum pressure. The wedge impacts the granules on the left and displaces them to the right from their starting positions (+). Overlapping colors denote results from different, nominally identical, experiments

profiles associated with the confined experiments are similar and cross the horizontal axis sooner than their unconfined counterparts, indicating that the confining pressure restricts the forward motion of the wedge.

Calibration of Membrane Properties

Modeling the membrane with high fidelity is a challenging task in our discrete element formulation as the membrane conforms to the sides of the spheres in the outer periphery of the specimen and the polymer membrane material can have a highly nonlinear constitutive response. In addition, during impact, the membrane stretches and changes the area of contact with the granules, which in turn alters the frictional dissipation associated with the granule/membrane interaction. To achieve a reasonable comparison with experiments, our model includes a simplified description of the lateral confining effect of the membrane and the energy dissipation stemming from the viscous response of the membrane and its frictional interaction with the granules.

As described earlier, this simplified model includes a spring-dashpot model attached to the sides of the array, i.e, to the granules that are not in contact with the incident or transmission plates, as was shown schematically in Fig. 5(b). The spring stiffness, k, and dashpot dissipation coefficient, c, representing the confining and dissipative effects of the membrane, respectively, are then found with the aid of a parametric calibration study by minimizing the error, e, between the numerically ($v_{w,sim}$) and experimentally ($v_{w,exp}$) obtained evolution of the wedge velocity. This error measure is defined as

$$e = \int_0^{t_{\max}} \sqrt{\left(v_{w,exp} - v_{w,sim}\right)^2}dt \tag{9}$$

where the bounds of the integral are based on the wedge velocity profiles shown in Fig. 8 with t_{max} denoting the time at which the wedge stops its forward motion. Contour plots of the dependence of e on the membrane parameters k and c are presented in Fig. 9. As apparent there, the optimum value of the spring stiffness k is found to be 7000 *N/m* for the confined

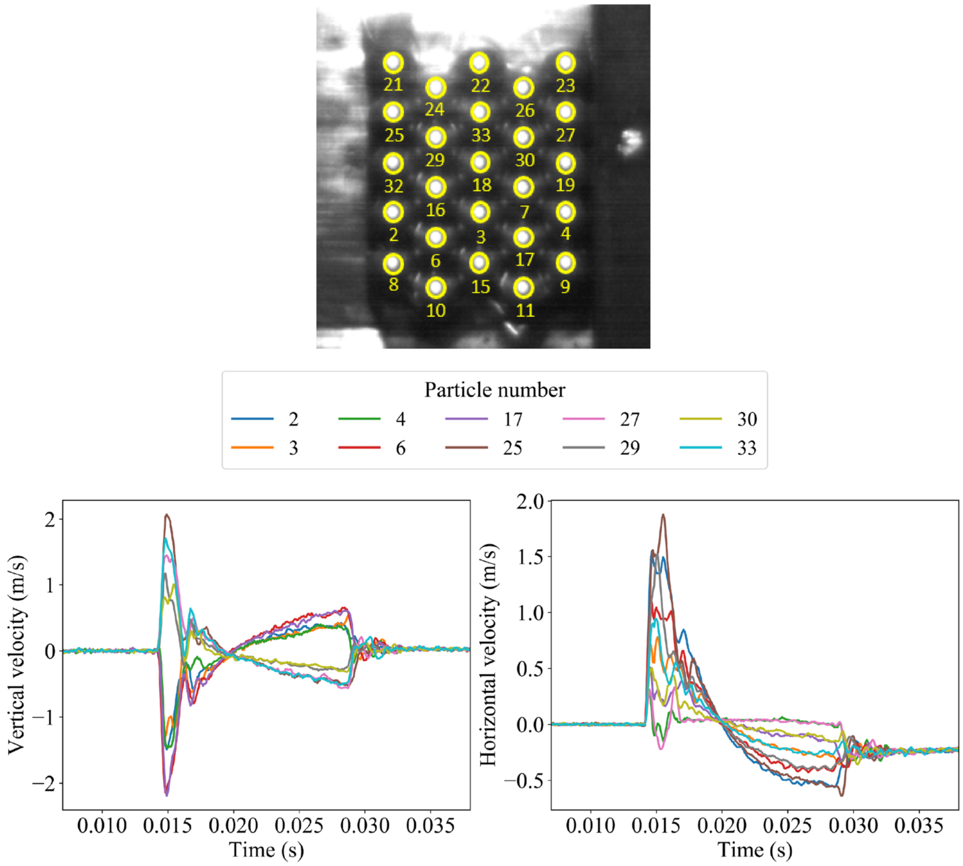

Fig. 7 x and y velocities of granules selected from the top image for a specimen with 70 *kPa* vacuum pressure

case (irrespective of the vacuum pressure) and 3000 *N/m* for the unconfined case. This observation agrees with quasi-static bending tests, which reported an increase in bending stiffness with vacuum pressure [32]. As for the optimal c value, both the confined and unconfined cases yield a value of 2 *Ns/m*. Simulated evolutions of the wedge velocity and granule trajectories obtained with these optimal parameters are presented in Fig. 10. The lower level of agreement in the granule trajectory predictions in the unconfined case could be attributed to the inability of the simplified spring-dashpot model to handle the larger horizontal motion of the less constrained granules, or due to the presence of small gaps between the membrane and adjacent granules before impact in experiments. The latter would imply that the effect of the membrane activates at a slightly later time after impact once the granules impinge on the membrane.

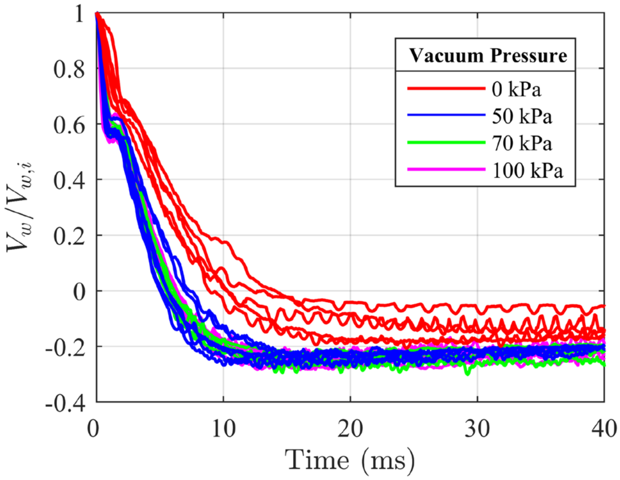

Fig. 8 Evolution of the wedge velocity (V_w) normalized by its initial value ($V_{w,i}$) measured before impact for varying levels of vacuum pressure

Lateral Expansion

In this subsection we quantify the lateral expansion of the specimen observed in Fig. 6 by computing the ratio of lateral strain to axial strain, η, based on granular trajectories. This ratio will be denoted as the lateral expansion ratio even though its definition is similar to the Poisson's ratio of a continuum material. The reason being that the limited dimensions of the array makes it unlikely to assume that the values taken by η could be generalized to be representative as a material property for a granular array of any size or subjected to different boundary conditions.

If we consider four spheres of interest in a rhombic arrangement with two spheres each in the horizontal (l and

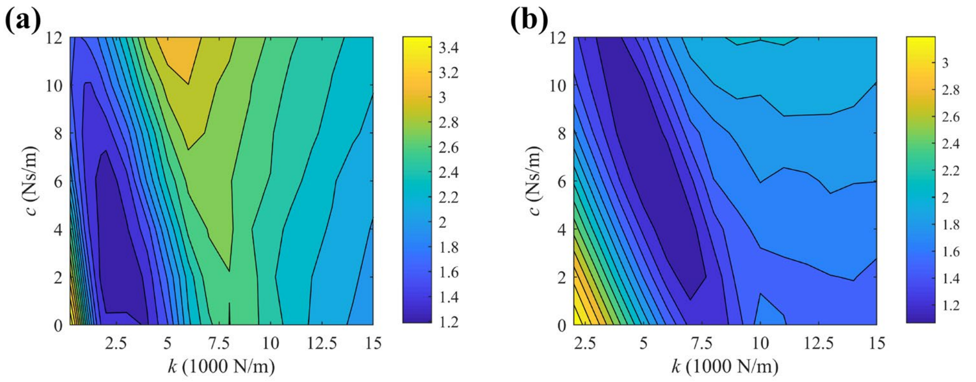

Fig. 9 Contours for the error measure defined in Eq. (9) for different values of k and c in the parametric study for (**a**) unconfined case, for which the optimal k and c are 3000 *N/m* and 2 *Ns/m*, respectively, and (**b**) 70 *kPa* confined case, for which the optimal k and c are 7000 *N/m* and 2 *Ns/m*, respectively. Results obtained for different vacuum pressures yield similar contour plots, hence only one representative result is shown

r) and vertical directions (t and b), η can be extracted by comparing the vertical and lateral contractions of the granules. For example, using granule number 32 (l), 19 (r), 33 (t) and 3 (b) in Fig. 7, the lateral expansion ratio can be expressed as

$$\eta = -\frac{\dfrac{u_{y,33} - u_{y,3}}{y_{0,33} - y_{0,3}}}{\dfrac{u_{x,19} - u_{x,32}}{x_{0,19} - x_{0,32}}}, \tag{10}$$

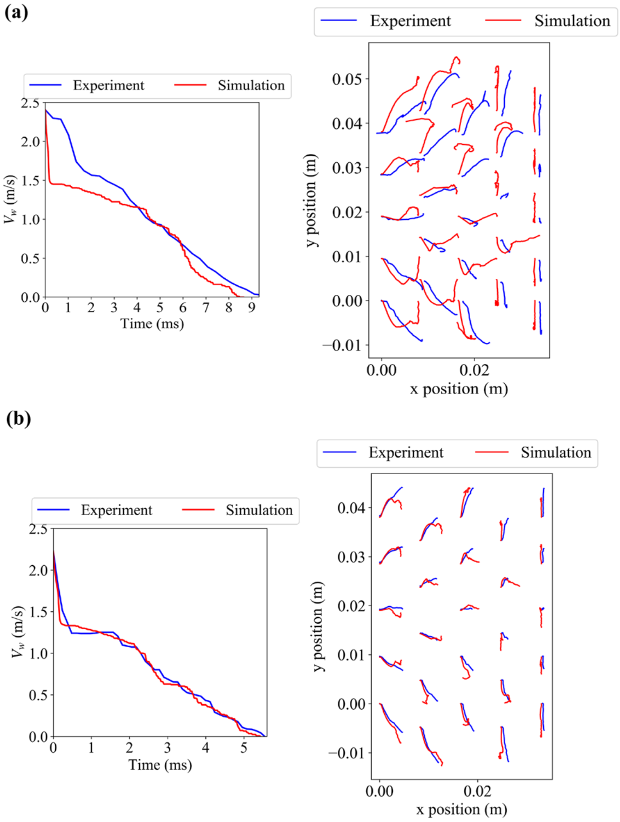

Fig. 10 Experimental and numerical evolution of the wedge velocity and particle trajectories for the unconfined (**a**) and confined (70 *kPa*) (**b**) cases. The adopted simulation parameters are the optimal parameter combination extracted in Fig. 9

where u_x and u_y are the respective x and y displacements, and x_0 and y_0 are the respective initial positions. This definition yields similar results when applied to the nearest and next nearest neighbors specified in a rhombic configuration.

Figure 11 shows the experimentally and numerically obtained lateral expansion ratio as a function of wedge displacement. As evident there is a sharp increase in η in the beginning as the forces are distributed outward along networks at 60° from the plane of loading in a hexagonal close pack system. The maximum value of η is well beyond 1 which implies that there is an increase in the area of the specimen. This phenomenon is due to dilatancy as the granular layers slide past each other [38]. The rise in η gradually decreases as the interstitial gaps open up during granular rearrangement, thereby offering less resistance to granular motion in the loading direction. Also apparent is the fact that the higher vacuum pressure experiments yield a slightly lower value of η in the early stages of the impact event, which agrees

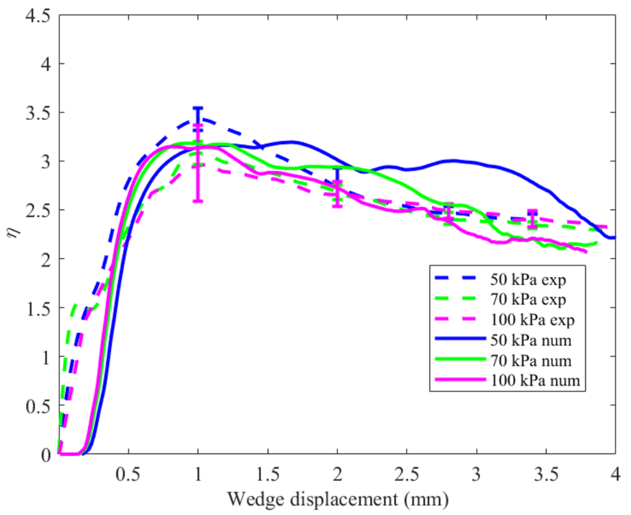

Fig. 11 Lateral expansion ratio (η) versus wedge displacement from experimental data and simulations. The presented results are averaged over multiple trials conducted at a given pressure level, for both experiments (dashed) and simulations (filled). Scatter bars indicate the standard deviation between trials

intuitively with the inverse relationship between lateral motion and the confining pressure. As the wedge displacement increases, all cases converge to the same value of η as inertial effects become less significant. The experimental and simulation results agree well with each other after an initial displacement of around 0.3 *mm*, with the early discrepancy attributed to the inability of the virtual model to capture the experiments immediately after impact (Fig. 10).

Energy Dissipation

One of the main objectives of this work is to determine how impact-induced plastic dissipation is affected by the confining pressure. The total energy of the system prior to impact is the kinetic energy of the wedge. During impact, elasto-plastic waves traverse the array increasing the kinetic energy of the granular array while simultaneously dissipating energy by plastic dissipation at granule contact points, by friction both between granules and between granules and membrane, and by viscous losses in the membrane itself. Figure 12(a) illustrates the evolution of the kinetic energy of the wedge and the sum of kinetic energies of all the granules extracted from the particle tracking measurements of each granule's instantaneous velocity (Fig. 7). As apparent there, the maximum kinetic energy of the granules is only a fraction of the wedge energy with the remainder predominantly converted to strain energy of the membrane, and dissipated through plastic deformation and frictional contact. To support these results, simulations are used to obtain the evolution of energy transfer between the wedge and granular array (Fig. 12(b)) which cannot be extracted experimentally. The instantaneous strain energy at a contact (E_s), work done by pressure on boundary granules ($E_{wd,vacuum}$), spring potential energy ($E_{mem,pot}$) and dissipated viscous energy ($E_{mem,visc}$) are calculated using the following equations

$$
\begin{aligned}
E_s &= \begin{cases} \int_0^\delta F_l \mathrm{d}\delta, \ \delta \le \delta_y, \\ \int_{\delta_r}^\delta F_u \mathrm{d}\delta \ \ \delta \ge \delta_y \end{cases} \\
E_{wd,vacuum} &= R \cdot u \\
E_{mem,pot} &= 0.5ku_y^2 \\
E_{mem,vis} &= \int_0^t cv_y^2 dt.
\end{aligned}
\tag{11}
$$

Here v_y refers to the y velocity of the granule attached to the dashpot. It can be seen that plastic dissipation is an incremental process with intermittent jumps throughout the duration of the impact. Another observation is that between these jumps, granular strain energy is negligible which implies that the granules are non-contacting or carrying very low loads. Eventually at maximum compression once the kinetic energies of both the wedge and granules drop to zero, the greatest plastic dissipation and membrane potential energy are realized. Although the trends of the kinetic energies for both the experiments and simulations are similar, the experiments show a lower maximum granular kinetic energy due to simulations being frictionless and having a simplistic membrane model.

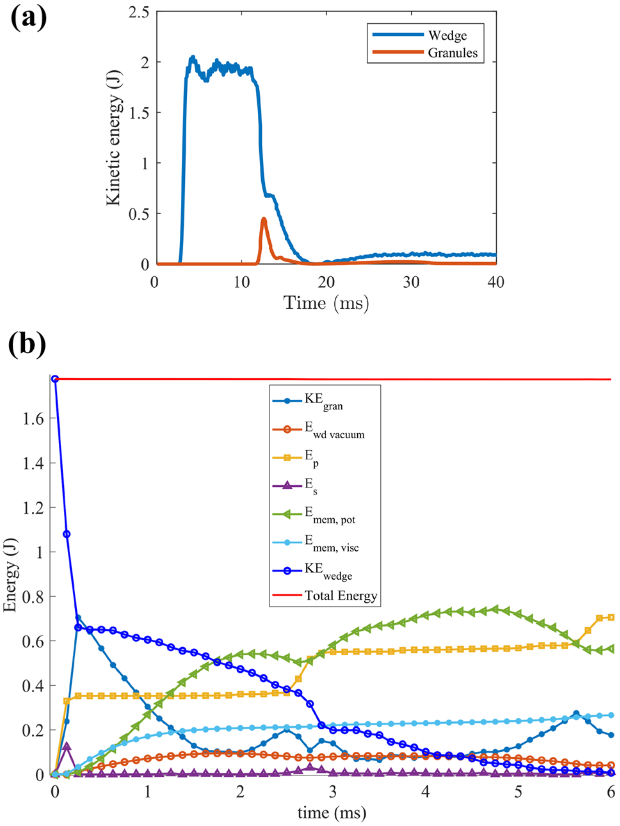

Fig. 12 (**a**) Kinetic energies of the wedge and granules for an experiment with a vacuum pressure of 50 *kPa*. The timescale is referenced to the time at which the wedge impacts the specimen. The kinetic energy before impact indicates the energy which the wedge obtains from the SHPB. (**b**) Energy evolution of the different constituents as obtained from the simulations for the same 50 *kPa* experiment

The compression phase is followed by the restitution phase when the strain energy of the membrane gets predominantly converted back into kinetic energy of the wedge which gets pushed back. Additional plastic dissipation is not expected to occur during restitution as the granules move much slowly, and are thus unlikely to generate forces comparable to the maximum forces in compression. The net input energy is thus the difference in the kinetic energy of the wedge before and after impact.

The results for the dissipated plastic energy, obtained using the procedure outlined in Experimental setup based on a post-mortem measurements of residual contact areas on the granules, are shown normalized by the net input energy in Fig. 13. These results reveal that having a non-zero vacuum pressure creates a jump in the dissipated plastic energy. However, no noticeable increase in dissipation with the vacuum pressure is observed in the confined regime. The scatter bars indicate the deviation of results between trials due to differences in impact velocity and errors associated with dimple area measurement. It is also apparent that, even though the simulations do not capture friction between the beads, the dissipation ratios show close agreement between the experiment and simulations for the confined cases, which suggests that friction plays a secondary role in this state. The slightly higher dissipation in the simulations could be due to the fact the interaction between the wedge and membrane is not included in the simulations leading to more energy transmitted to the array than in the experiment. However, the reasons for the substantially higher dissipation obtained in the unconfined simulations could be twofold. It could be first attributed to the model's inability to capture frictional dissipation due to the relative motion between granules, which is likely more prominent in the unconfined case. Another reason could be due to the existence of small gaps between the granules and the membrane as mentioned in Calibration of Membrane Properties. If small gaps exist, the simulation protocol would artificially stiffen the array enabling more plastic dissipation. Simulations conducted on unconfined experiments without a membrane ($k = c = 0$) verify this claim as shown by the green data point in Fig. 13. Here we assume the net input energy to be the same as that of the experiments, but the dissipated plastic energy is generated under no membrane conditions. The results indicate that plastic dissipation in unconfined experiments occurs during the initial impact as the absence of the membrane prevents further granular interaction (Fig. 2(a)). The cessation of plastic dissipation even after the granules start to push against the membrane could be due to the granules being scattered after the first impact to create networks which transmit energy outwards to the membrane.

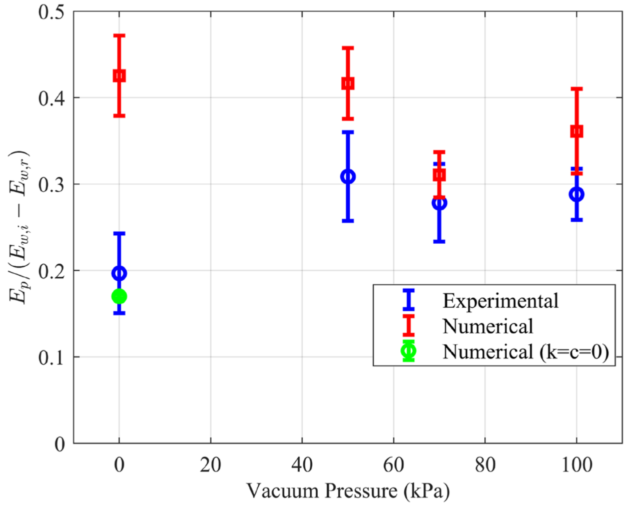

Fig. 13 Dissipated plastic energy (normalized by the input energy) vs. the vacuum pressure: comparison between experiments and simulations. The scatter bars denote the standard deviation between trials with the 0 *kPa*, 50 *kPa*, 70 *kPa*, and 100 *kPa* experiments respectively involving 5,6,4,and 5 trials. Additional simulations performed without the spring-dashpot for the unconfined cases show better agreement with experiments

The relative independence of the plastic dissipation on the vacuum pressure in the confined regime can be linked to the clustering of data for the wedge velocity and lateral expansion ratio described in previous sections. This observation can be explained as follows: due to the ordered nature of the hexagonally packed array and the fact that the forces generated at impact are much larger than the forces holding the array together, the specimen (irrespective of the vacuum pressure) gets briefly disjointed making the granules lose contact with each other during initial wave propagation. Although the resolution of the high-speed camera is not high enough to observe this loss of contact, this effect could make the plastic dissipation and lateral expansion results indistinguishable between the different levels of confinement as the momentary loss in contact network leads to an inability to transmit contact forces and in turn to dissipate energy.

Numerical Investigation of Effects of Array Size

The above choice of a 5 × 5 granular array which was studied both experimentally and numerically was primarily driven by physical consideration and space limitation in the experimental set-up. To address the question of whether the results observed so far can be generalized to larger arrays, we have performed numerical simulations on larger array sizes using the same modeling approach that has produced reliable results for the 5 × 5 case. These simulations were conducted on unconfined (no vacuum and no membrane) and confined symmetric square arrays to investigate the effect that array size has on trajectories and dissipation. Unlike the 5 × 5 packing which has symmetry only about the vertical (y axis) mid-plane at the center of the packing, the square arrays have symmetry about the horizontal mid-plane (x axis) in the center as well. Having symmetry about both the x and y axes does not bias the way in which the array moves, and, as will be seen, allows for the results to be generalized. Since the energy dissipated by the dashpot is less significant compared to the energy stored in the spring (Fig. 12(b)), the effect of the dashpot is ignored in this analysis. In order to make comparisons amongst differently sized arrays, the mass of the impactor wedge is scaled linearly with the total mass of the granular array while keeping V_w at the median experimental V_w of 2.23 *m/s*. This scaling is easily derived from the conservation of energy and momentum involving the collision of two rigid bodies such that similar post impact velocities are obtained when the mass of one of the rigid bodies is changed.

Plotting the granular trajectories for an array containing 39 and 588 granules, top portion of Fig. 14, reveals a pattern in which the array particle motions occur within three regions moving in a symmetric manner about the horizontal plane of symmetry. The first region constitutes of two triangular blocks in the left half of the granular array which split up about the midpoint, and slide almost like a rigid portion along an angle moving in opposite directions. These blocks, which are collectively referred to here as the "shell", move around a diamond-shaped "core" whose particles exhibit far less motion. To the aft of the core are two smaller triangular sections, collectively referred to here as the "base", which constitute particles in contact with, or very near, the right-hand wall support. The base is flanked on the inner side by the core and on the outer side by the shell. This characteristic granular motion was observed for all array sizes simulated, and even the asymmetric 5 × 5 array shows these same three region types in Fig. 10, with each half of the shell and base containing a different number of granules since the 5 × 5 array is asymmetric.

The consistent trajectories which appear in each region irrespective of the array size motivates the discussion on the effect array size has on plastic dissipation. A map of the total amount of dissipated plastic energy *per granule* is presented in Fig. 14 illustrating the importance each starting granular position has on its energy dissipating capability. This map is obtained by equally distributing the final dissipated energy at a pairwise contact between two contacting granules, and summing over all contacts for a given granule. Comparing the location specific dissipated energy reveals that both the 39 and 588 granules systems show less plasticity on the lateral (top and bottom) edges of the array, and more dissipation in the core. A possible explanation for the latter is that the granules in the core move less as they are confined on all four sides, leading to increased compression and more plastic dissipation there. The asymmetry in plastic dissipation even though the arrays are symmetric is due to multiple wave reflections from the rigid transmission plate and wedge. These boundary reflections have been showed in Hertzian systems to cause perfectly symmetric packings to transcend to disorder over long durations [22].

Figure 15 quantifies these plastic dissipation results by tallying the average dissipated energy per granule in the three regions for different confining pressures and array sizes. It can be first observed that dissipation is independent of confining pressure apart from the fact that there is a jump in dissipation between an unconfined and confined array which agrees with the results shown in Fig. 13. The near four-fold increase in dissipation between the unconfined and confined array in Fig. 15, as opposed to the two-fold increase in the 5 × 5 packing, is due to the symmetric array having more support and these simulations having no viscous dissipation. Upon closer investigation, we observe that the core shows the most plastic dissipation, followed by the base and

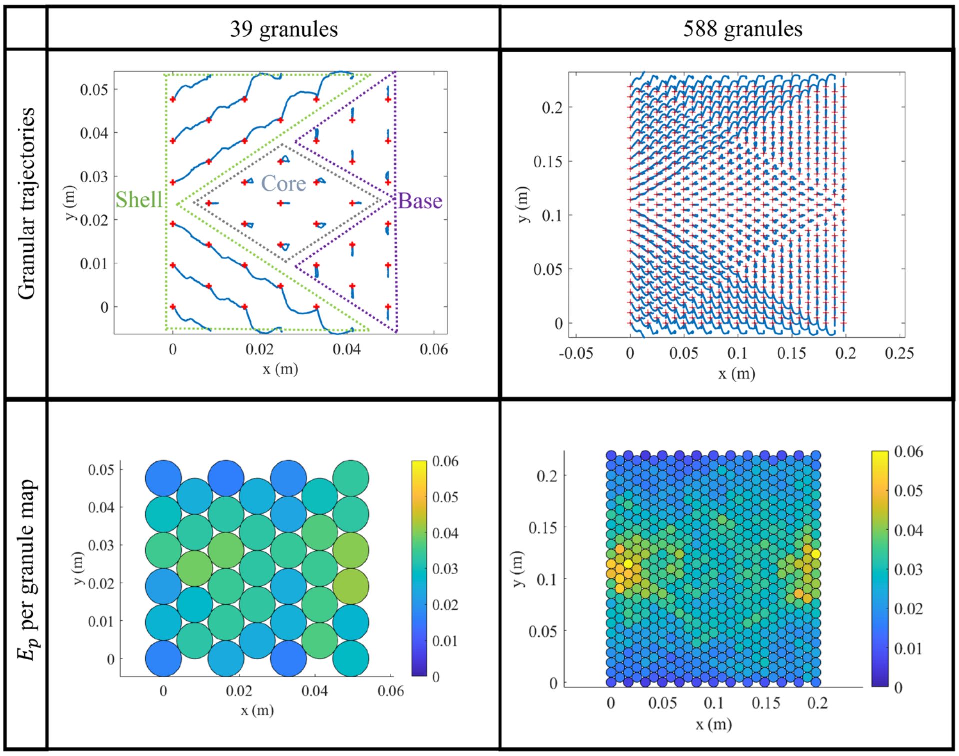

Fig. 14 Figure matrix showing the granular trajectories and plastic dissipation map for arrays containing 39 and 588 granules. The colorbar denotes the energy dissipated per granule. + show the starting positions of trajectories

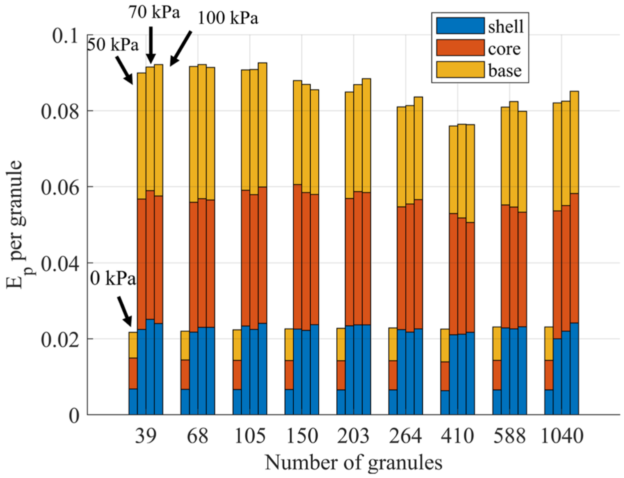

Fig. 15 Stacked bar plot of the plastic dissipation per granule in each region for differently sized square packings. Each group has 4 columns which denote the confining pressure as annotated in the figure

shell. Increasing the array size shows a slight decrease in the aggregate dissipated energy in the three regions (11% between 39 and 588 granules) primarily due to dissipation decreasing in the base. Given the consistency in the partitioning of both trajectories and plasticity in the three regions with varying array size, it is plausible that the experimental observations will carry over to for larger hexagonally packed granular systems.

Conclusions

In this manuscript, we have presented an experimental and numerical investigation of the impact response of a vacuum-induced, confined granular array. The array consists of brass spheres enclosed in a polymer membrane, which upon the application of vacuum promotes a transition from an unconfined fluid-like state to that of a confined rigid state. Experiments have been conducted on 2D hexagonally packed arrays using a split Hopkinson pressure bar-type loading device while recording the impact event using high-speed imaging. Particle tracking has been implemented on the high-speed photography footage to track the motion of granules, while post-mortem analysis of the granular surfaces after impact have quantified the energy dissipated due to plasticity.

The confined experiments have shown similar and shorter trajectories between trials, which contrast with the substantially larger displacements observed in the unconfined experiments. During loading, there is a reversible change in the granular configuration for confined experiments, which is recovered when the specimen is unloaded. To complement the experiments, discrete element simulations have been performed with a frictionless, elasto-plastic contact law for the granules and a simplified linear spring-dashpot model of the membrane. The numerical model has been calibrated for the membrane stiffness (k) and damping coefficient (c) through a comparison with the experimental evolution of the wedge velocity. The model has then been validated against the trajectories of the granules during the impact event, and the evolution of the effective lateral expansion ratio in the confined states extracted from the relative motion of adjacent particles. The energy dissipated due to plasticity has been found to be higher in confined experiments, which suggests that the transition enhances plastic dissipation. However, there was no noticeable increase in dissipation with vacuum pressure in the range investigated in this study. The lower agreement between simulations and experiments for the unconfined case suggests the need for a more realistic model for the membrane and its frictional interaction with the brass particles. Finally, simulations performed on larger symmetric arrays showed that the results for trajectories and plastic dissipation are generally size independent as noted by the consistency in these results irrespective of the array size.

Acknowledgements This material is based upon work supported by the National Science Foundation under grant number NSF CMMI 17-61243.

Funding This work was supported by the National Science Foundation under grant number NSF CMMI 17-61243.

Declarations

Conflicts of Interest The authors declare that they have no conflict of interest.

References

1. Sen S, Manciu F, Manciu M (2001) Thermalizing an impulse. Physica A: Statistical Mechanics and its Applications 299(3):551–558
2. Nakagawa M, Agui JH, Wu DT, Extramiana DV (2003) Impulse dispersion in a tapered granular chain. Granul Matter 4(4):167–174
3. Doney R, Sen S (2006) Decorated, tapered, and highly nonlinear granular chain. Phys Rev E 97:155502
4. Leonard A, Ponson L, Daraio C (2014) Wave mitigation in ordered networks of granular chains. J Mech Phys Solids 73:103–117
5. Fu K, Zhao Z, Jin L (2019) Programmable granular metamaterials for reusable energy absorption. Adv Funct Mater 29(32):1901258
6. Yang J, Dunatunga S, Daraio C (2012) Amplitude-dependent attenuation of compressive waves in curved granular crystals constrained by elastic guides. Acta Mech 223:549–562
7. Brilliantov NV, Spahn F, Hertzsch J, Pöschel T (1996) Model for collisions in granular gases. Phys Rev E 53:5382–5392
8. Kuwabara G, Kono K (1987) Restitution coefficient in a collision between two spheres. Jpn J Appl Phys 26(Part 1, No. 8):1230–1233
9. Bourrier F, Nicot F, Darve F (2008) Physical processes within a 2D granular layer during an impact. Granul Matter 10(6):415–437
10. Karanjgaokar N (2017) Evaluation of energy contributions using inter-particle forces in granular materials under impact loading. Granul Matter 19(2):36

11. Pal RK, Geubelle PH (2014) Impact response of elasto-plastic granular and continuum media: a comparative study. Mech Mater 73:38–50
12. Nesterenko VF (1983) Propagation of nonlinear compression pulses in granular media. J Appl Mech Tech Phys 24(5):733–743
13. Sinkovits RS, Sen S (1995) Nonlinear dynamics in granular columns. Phys Rev Lett 74:2686–2689
14. Sen S, Sinkovits RS (1996) Sound propagation in impure granular columns. Phys Rev E 54:6857–6865
15. Coste C, Falcon E, Fauve S (1997) Solitary waves in a chain of beads under Hertz contact. Phys Rev E 56:6104–6117
16. Sen S, Manciu M, Sinkovits RS, Hurd AJ (2001) Nonlinear acoustics in granular assemblies. Granul Matter 3(1):33–39
17. Daraio C, Nesterenko VF, Herbold EB, Jin S (2005) Strongly nonlinear waves in a chain of Teflon beads. Phys Rev E 72(1):016603
18. Jayaprakash KR, Starosvetsky Y, Vakakis AF (2011) New family of solitary waves in granular dimer chains with no precompression. Phys Rev E 83(3):036606
19. Porter MA, Daraio C, Herbold EB, Szelengowicz I, Kevrekidis PG (2008) Highly nonlinear solitary waves in periodic dimer granular chains. Phys Rev E 77(1):015601
20. Awasthi AP, Smith KJ, Geubelle PH, Lambros J (2012) Propagation of solitary waves in 2D granular media: a numerical study. Mech Mater 54:100–112
21. Manjunath M, Awasthi AP, Geubelle PH (2014) Plane wave propagation in 2D and 3D monodisperse periodic granular media. Granul Matter 16(1):141–150
22. Hua T, Van Gorder RA (2019) Wave propagation and pattern formation in two-dimensional hexagonally packed granular crystals under various configurations. Granul Matter 21(3):3
23. Sadd MH, Tai Q, Shukla A (1993) Contact law effects on wave propagation in particulate materials using distinct element modeling. Int J Non Linear Mech 28(2):251–265
24. Shukla A, Sadd MH, Xu Y, Tai Q (1993) Influence of loading pulse duration on dynamic load transfer in a simulated granular medium. J Mech Phys Solids 41(11):1795–1808
25. Wang E, On T, Lambros J (2013) An experimental study of the dynamic elasto-plastic contact behavior of dimer metallic granules. Exp Mech 53:883–892
26. Wang E, Geubelle PH, Lambros J (2013) An experimental study of the dynamic elasto-plastic contact behavior of metallic granules. J Appl Mech 80(2):021009
27. On T, LaVigne P, Lambros J (2014) Development of plastic nonlinear waves in one-dimensional ductile granular chains under impact loading. Mech Mater 68:29–37
28. Burgoyne HA, Daraio C (2015) Elastic-plastic wave propagation in uniform and periodic granular chains. J Appl Mech 82(8):081002
29. Burgoyne HA, Newman JA, Jackson WC, Daraio C (2015) Guided impact mitigation in 2D and 3D granular crystals. Procedia Engineering 103:52–59
30. Waymel RF, Wang E, Awasthi A, Geubelle PH, Lambros J (2018) Propagation and dissipation of elasto-plastic stress waves in two-dimensional ordered granular media. J Mech Phys Solids 120:117–131
31. Brown E, Rodenberg N, Amend J, Mozeika A, Steltz E, Zakin MR, Lipson H, Jaeger HM (2010) Universal robotic gripper based on the jamming of granular material. Proc Natl Acad Sci 107(44):18809–18814
32. Jiang A, Ranzani T, Gerboni G, Lekstutyte L, Althoefer K, Dasgupta P, Nanayakkara T (2014) Robotic granular jamming: does the membrane matter? Soft Rob 1(3):192–201
33. Allan D, Caswell T, Keim N, van der Wel C (2016) Trackpy: Trackpy v0.3.2.
34. van der Walt S, Schönberger JL, Nunez-Iglesias J, Boulogne F, Warner JD, Yager N, Gouillart E, Yu T, The Scikit-image Contributors (2014) Scikit-image: image processing in Python. PeerJ 2:e453
35. Pal RK, Awasthi AP, Geubelle PH (2013) Wave propagation in elasto-plastic granular systems. Granul Matter 15(6):747–758
36. Thornton C (1997) Coefficient of restitution for collinear collisions of clastic-perfectly plastic spheres. J Appl Mech 64(2):383–386
37. Nicot F, Hadda N, Guessasma M, Fortin J, Millet O (2013) On the definition of the stress tensor in granular media. Int J Solids Struct 50(14):2508–2517
38. Andreotti B, Forterre Y, Pouliquen O (2013) Granular media: between fluid and solid. Cambridge University Press